# Microstructural Evolution and Intermetallic Formation in Zn-3Mg (wt.%) Powder Mixture Processed by High-Pressure Torsion

Tanzilur Rahman<sup>1</sup>, Hakan Yilmazer<sup>2,3</sup>, Burak Dikici<sup>4</sup>, Kaveh Edalati<sup>5</sup>, Jonathan D. Poplawsky<sup>6</sup> and Carl J. Boehlert<sup>1</sup>

- 1. Department of Chemical Engineering and Materials Science, Michigan State University, East Lansing, USA
- 2. Department of Metallurgical and Materials Engineering, Yildiz Technical University, Esenler, Istanbul, Turkey
- 3. Health Biotechnology Joint Research and Application Center of Excellence, Esenler, Istanbul, Turkey
- 4. Ataturk University, Faculty of Engineering, Department of Metallurgical and Materials Engineering, Erzurum, Turkey
- 5. WPI, International Institute for Carbon-Neutral Energy Research (WPI-I2CNER), Kyushu University, Fukuoka, Japan
- 6. Center for Nanophase Materials Sciences, Oak Ridge National Laboratory, Oak Ridge, TN, USA

#### Abstract

Severe plastic deformation (SPD) techniques have been used extensively over the past 40 years for producing strong metals and alloys. High-pressure torsion (HPT) is one of the most promising SPD techniques for achieving high strength through nanoscale grain refinement and phase transformation. In this research, a mixture of pure zinc (Zn) and magnesium (Mg) powders, Zn-3Mg (wt.%), was HPT-processed under a pressure of 6 GPa for 1, 5, 10, 20, and 30 turns at room temperature to achieve a high strength biodegradable material. In order to understand the effects of pre-consolidation on the resulting microstructure and hardness, HPT processing was performed on loose powders placed in the die and also on a pre-compacted powder mixture and characterized by X-ray diffraction, scanning electron microscopy, atom probe tomography, and Vickers microhardness. In both cases, the microstructures contained nanoscale grains, and stable and metastable strain-induced intermetallics, but an unusual softening appeared at large shear strains.

Grain size, grain morphology, and the formation of different intermetallics were analyzed to explain the unusual hardness distribution, and it was found that an inverse Hall-Petch relationship between hardness and grain size exists. It is suggested that thermally-activated phenomena such as grain boundary sliding contribute to the strain-induced softening of this nano-structured biomaterial due to its low melting point. The current results are compared with those for HPT-processed cast alloys and hybrids of the same composition.

Keywords: High-pressure torsion, zinc, magnesium, Zn-Mg intermetallics, Ultrafine-grained biomaterial

#### 1. Introduction

High-pressure torsion (HPT) has been used to process bulk nano-structured pure metals and alloys to significantly improve their hardness and strength during the past decades [1]–[13]. This process, which is a severe plastic deformation (SPD) method, simultaneously applies torsional shear strain and high hydrostatic pressure on relatively small (usually 10mm diameter) disk samples. Previous research in this area has focused on understanding grain refinement mechanisms that lead to the increase of mechanical strength and hardness in a wide variety of pure metals and alloys [3], [4], [14], [15]. Numerous studies showed that despite the microstructural evolution and phase transitions in the early stages of straining, the microstructural features become saturated at large strain, where a steady-state is achieved, and the hardness values remain relatively constant [14], [16]. Although the occurrence of steady-states at large strains is expected in single-phase metals [5], [17] because of the contribution of dynamic recovery [18], dynamic recrystallization [19], grain-boundary rotation [20], and/or grain-boundary migration [16], it is still not well understood why and when a steady-state is reached in multiple-phase materials with immiscible phases [21]–[24].

HPT is also one of the most efficient techniques for consolidating metallic particles because the processing is generally conducted both under a high hydrostatic compressive stress and with high shear deformation. These conditions lead to the deformation and bonding of the particles while preventing cracking. HPT has been used to successfully consolidate various pure metals [25]–[28], alloys [29]–[32], metallic glasses [33], ceramics powders [34]–[37], and high entropy alloys [38]–[40] at low temperatures. More attention should be paid to developing this technique to understand the resulting microstructural evolution and associated mechanical properties.

Zn-Mg alloys are excellent candidates for biodegradable biomedical implant applications due to the relatively poor corrosion resistances in body fluids of Zn and Mg and their abundance in the human body [41]. HPT processing results in remarkable increases in hardness and tensile strength of Zn-Mg cast alloys and hybrids [1]–[3], [13], and after annealing, they exhibit an attractive balance of strength and elongation to failure ( $\varepsilon_f$ ) [1]. Hernandez-Escobar et al. showed that Mg contents greater than 3 wt.% do not offer a significantly higher hardness for 3-30 wt.% Mg [42], and Zn-3Mg (wt.%) exhibits better corrosion resistance in comparison to pure Zn and other Zn-Mg alloys [43]. Zn-3Mg (wt.%) alloys HPT processed from powders have yet to be examined. The focus of the current work is on comparing the microstructure and hardness of powder-processed HPT disks with similar disks processed from alloys as well as hybrids. In particular, the different hardness distributions of these multiple-phase materials and their steady-state behavior are discussed. The study attempts to find out if the significant grain refinement resulting from the HPT processing of powders is beneficial to enhance the strength of Zn-Mg biomaterials.

#### 2. Experimental Procedures

Commercially available pure zinc (Zn) powder of 98.8% purity and 91 micrometers (µm) average particle size was purchased from Goodfellow Corporation (Coraopolis, PA). Pure magnesium

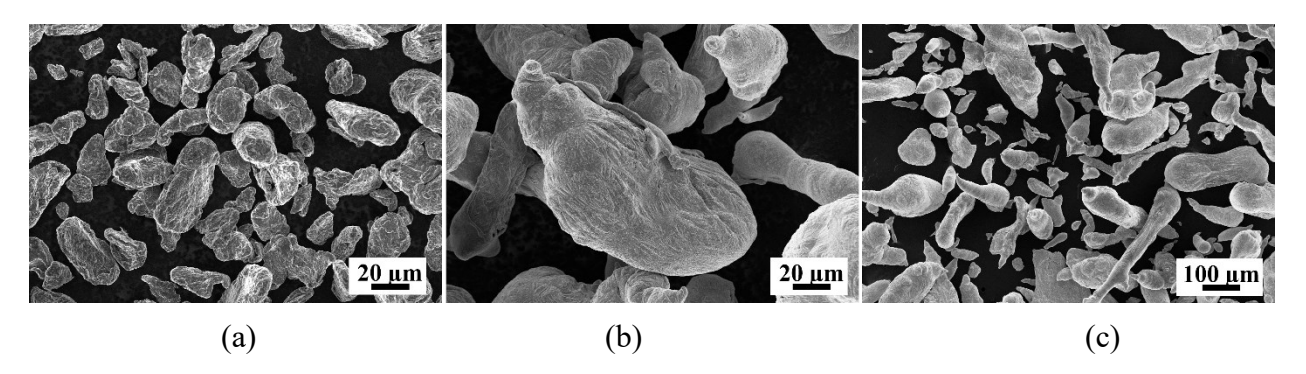


Figure 1. SE-SEM images of a) Mg powders and b) Zn powders at same magnification, and c) Zn powders at a lower magnification.

(Mg) powder of 99.8% purity and 21 µm average size was purchased from Goodfellow Cambridge

Limited (England). The powders were mixed with an eccentric blender for 2 hours under an inert gas atmosphere at a composition of 97% Zn and 3% Mg (mass ratio). Secondary electron (SE) scanning electron microscopy (SEM) images of Zn and Mg powders before HPT are shown in Figure 1. HPT was carried out in the open-air at room temperature under the pressure of 6 GPa and a rotational speed of 1 rpm in a quasi-constrained condition to manufacture disks. The number of HPT turns were 1, 5, 10, 20, and 30 for loose powders after mixing (will be referred to as 'loose powder HPT disks' from now onwards), and 1, 5, 10, and 30 for powders that were compacted into a bulk form under a pressure of 450 MPa for 10 minutes using a hydraulic press before HPT (will be referred as 'compact powder HPT disks' from now onwards). The HPT processing of both the loose powders and compact powders resulted in disk-shaped samples of 10 mm diameter with the thickness varying from 0.54 mm to 0.74 mm.

The density of the HPT disks was determined by the Archimedes method according to the ASTM B311 [44]. Precisa 205A SCS precision weighing ( $\pm 0.01$  mg) kit was used for the measurements. The measurements were repeated three times to determine the average. The density of the bulk form of the compacted powder before HPT was 5.65 g/cm<sup>3</sup>.

#### 2.1 Microstructural Characterization

All the disks were cut in half along the diameter into two semi-circular shapes. The cross-section of each disk was mirror polished for microstructural characterization and microhardness measurements. The metallographic sample preparation techniques used are described in [2]. A Tescan Mira3 FEG-SEM combined with energy-dispersive spectroscopy (EDS) was used to capture secondary electron (SE) and backscattered electron (BSE) images from the cross-sections of HPT-processed disks at the center and various locations away from the center. 20 kV voltage and working distances between 9 and 11 mm were used while capturing the SEM images. At least

two SEM images were taken in both SE and BSE modes for every magnification chosen to avoid any bias in the measured microstructural parameters, such as grain size and phase volume fraction. Figure 2 shows a schematic of half of the HPT-processed disk and the corresponding thickness-radial plane from which the SEM images were taken. The linear intercept method was not applicable to measure the size of the intermetallic regions as they were not well-resolved in the SEM images. However, the resolvable Zn matrix grains were measured separately (one by one) using image J.[45] and then multiplied by 1.571 to convert the 2D grain size measurement to the spatial grain size according to ASTM E112-13 A2.10 [46].

EDS was performed to analyze the phase compositions in various areas of interest. The locations of interest were determined according to the equivalent strain ( $\varepsilon_{eq}$ ), also known as the von Mises strain, governed by the following equation [47]:

$$\varepsilon_{eq} = \frac{\gamma}{\sqrt{3}} = \frac{2\pi Nr}{h\sqrt{3}} \tag{1}$$

Where  $\gamma$  is shear strain, N is the number of HPT turns, r is the radial distance from the disk center, and h is the disk height or thickness. One average h value was used during the equivalent strain calculation for each set of samples (0.6 mm for the loose powder disks and 0.63 mm for the compact powder disks).

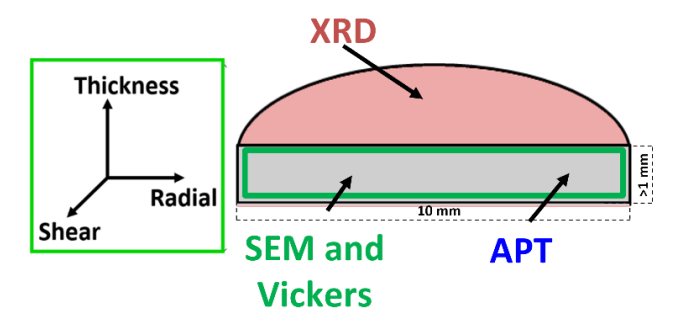


Figure 2. Schematic of half of an HPT-processed disk indicating areas where the microstructural characterization was performed.

X-ray diffraction (XRD) was carried out at the shear-radial plane of the semi-circular disk surface area using a high-resolution Rigaku Ultima IV XRD diffractometer (Figure 2). The top surface area of the semi-circular disk was ground slightly using SiC sandpapers. The Cu-K $\alpha$  radiation was used in a Bragg-Brentano configuration, with an accelerating voltage of 40 kV and a beam intensity of 44 mA, to gather the XRD patterns over a  $2\theta$  range of  $30^{\circ}$  to  $90^{\circ}$ . For all measurements, a step size of  $0.01^{\circ}$  and a scanning speed of  $3^{\circ}$ /min were selected.

For atom probe tomography (APT), needles from the HPT disks were prepared using a Thermo Fisher Nova 200 dual beam FIB-SEM using standard lift out and sharpening methods [48]. Two APT needles were prepared from the cross-section of two different compact powder HPT disks (Figure 2): the 10 turns HPT disk at a 4.5 mm distance from the center, and the 30 turns HPT disk at a 1.5 mm distance from the center. The APT experiments were run using a CAMECA Local Electrode Atom Probe (LEAP) 4000X HR in laser mode, with a laser pulse rate of 200 kHz, a laser pulse energy of 25-50 pJ, and a detection rate of 0.5%.

#### 2.2 Microhardness Testing

Vickers microhardness (HV) measurements were performed using a Clark CM-800AT microhardness tester at a load of 25 gf and a dwell time of 15 s. The microhardness was measured following a rectilinear grid pattern (32×4 matrix) at every 152 μm distance from the center along

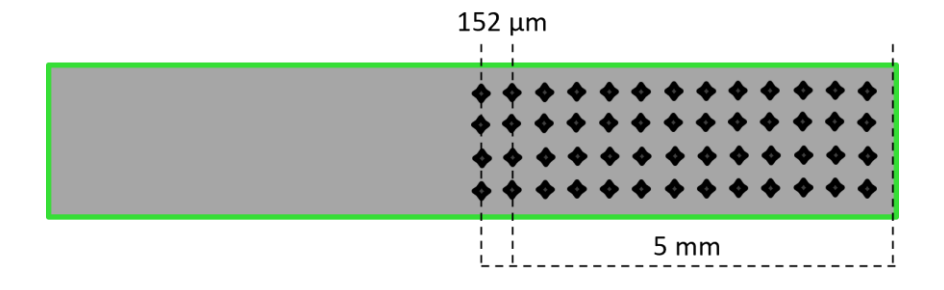


Figure 3. Schematic of the cross-section of an HPT processed disk indicating where the Vickers hardness characterization was performed.

the radius toward the edge of the semi-circular disk with equal spacing across the thickness of the cross-section (the thickness-radial plane in Figure 2). To obtain reliable HV data, it was confirmed that the sample surface was flat and perpendicular to the indenter. The tester load was chosen considering the indent diameter covered at least five grains. To prevent the effect of the residual plastic zone, the distance between two HV indents was maintained at least 2.5 times the diagonal of the indentation, or an indent and the edge of the test material, according to ASTM E92-17 [49]. A schematic of the microhardness indentation rectilinear grid pattern is shown in Figure 3.

#### 3. Results

The measured densities of both the loose and compact powder HPT disks are given in Table 1. The density of the loose powder HPT disks increased after 5 turns in comparison to 1 turn, but with the increased number of turns thereafter, the densities decreased gradually. The compact powder HPT disks exhibited a gradual density decrease with the increased number of turns.

Table 1. Average densities for the loose and compact powder HPT disks.

HPT Turn (N)	Density of loose powder HPT disks g/cm <sup>3</sup>	Density of compact powder HPT disks g/cm <sup>3</sup>
1	6.03	6.17
5	6.28	6.05
10	6.04	5.93
20	6.00	-
30	5.57	5.40

#### 3.1 Microstructural Characterization of the Loose Powder HPT Disks

Representative BSE-SEM images from each loose-powder HPT-processed disk at the center and edge (4.8 mm apart from the center) are shown in Figure 4 and Figure 5, respectively. The loose powders were consolidated into the Zn matrix phase (the bright matrix in Figure 4 and Figure 5)

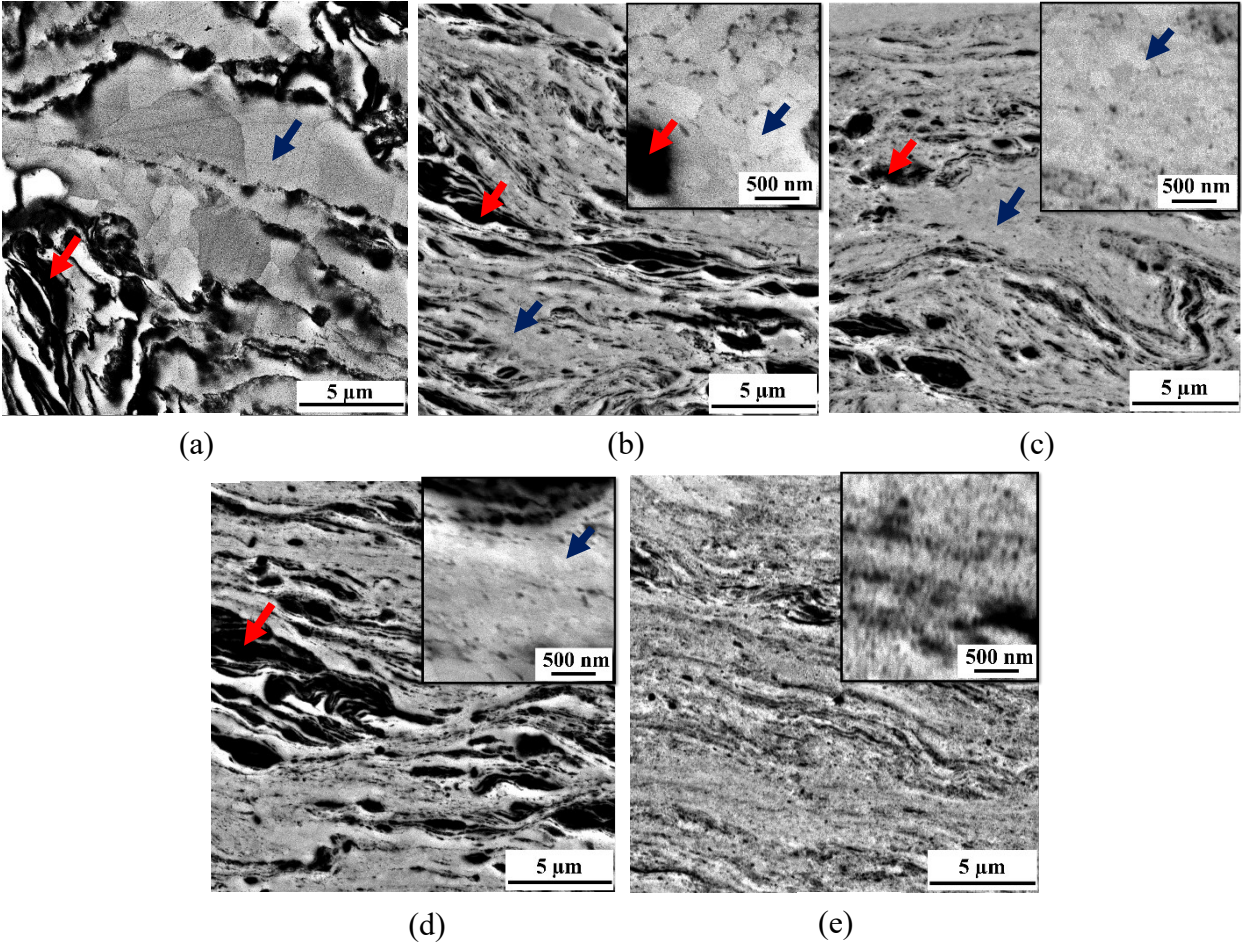


Figure 4. BSE-SEM images from the center of the cross-section of Zn-3Mg (wt.%) loose powder HPT disks after a) 1 turn, b) 5 turns, c) 10 turns, d) 20 turns, and e) 30 turns at same magnification. Red arrows indicate intermetallic phases and blue arrows indicate ultrafine Zn matrix grains.

and different Zn-Mg intermetallic compounds (the dark phases in Figure 4 and Figure 5), and the former decreased in grain size with increased equivalent strain. Table 2 summarizes the grain size of the Zn matrix, which could not be resolved for equivalent strains greater than 145, as a function of the number of turns, radius, and equivalent strain. Lamellar intermetallic regions of a maximum size of about 5  $\mu$ m in length and 2  $\mu$ m in width (as shown in Figure 4) were observed throughout the microstructure for equivalent strains up to 120. When the equivalent strain was greater than 120, the intermetallic regions were refined to nanometer size.

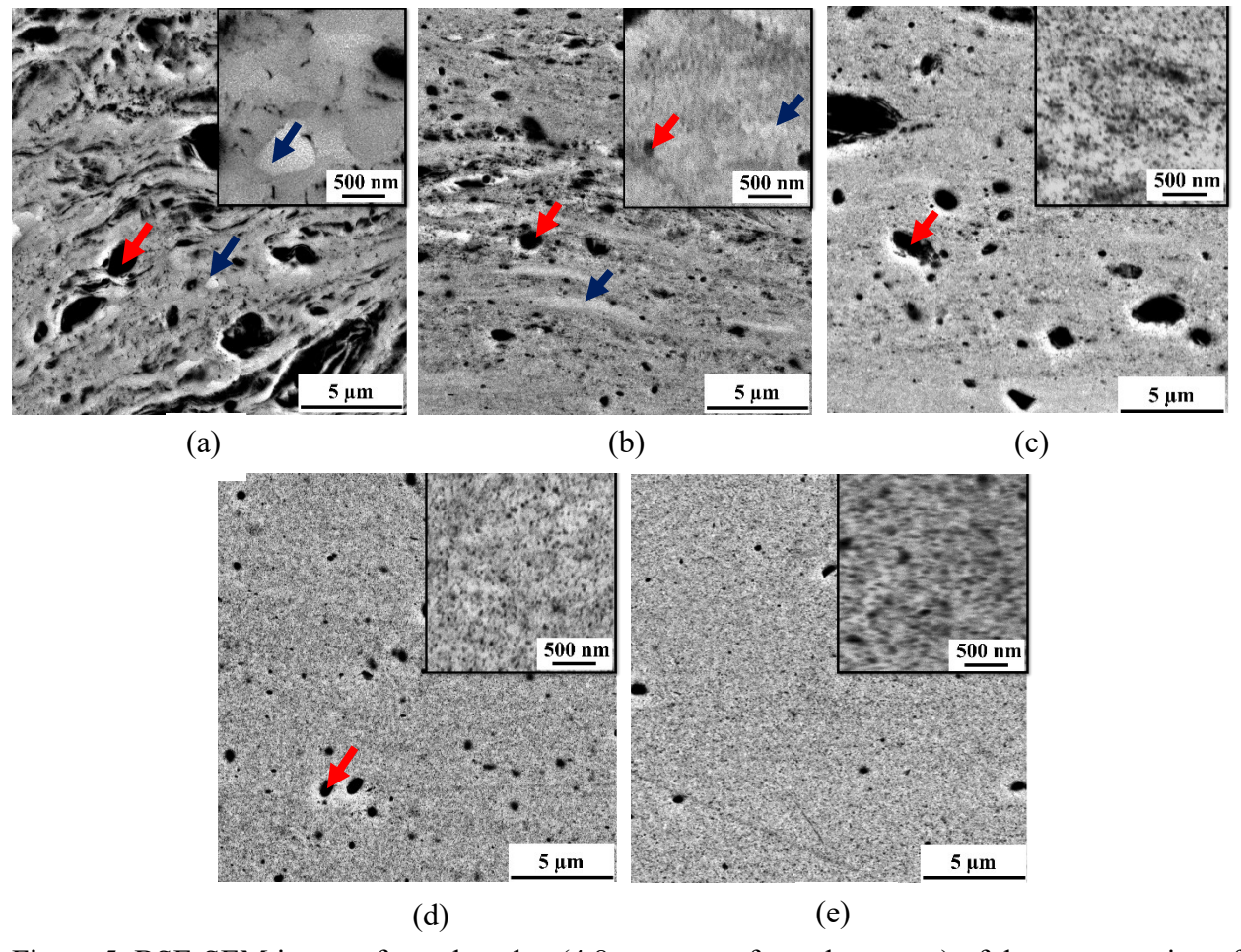


Figure 5. BSE-SEM images from the edge (4.8 mm apart from the center) of the cross-section of Zn-3Mg (wt.%) loose powder HPT disks after a) 1 turn, b) 5 turns, c) 10 turns, d) 20 turns, and e) 30 turns at same magnification. Red arrows indicate intermetallic phases and blue arrows indicate ultrafine Zn matrix grains.

Table 3 summarizes the EDS-measured compositions of the Zn matrix and Mg<sub>2</sub>Zn<sub>11</sub> and Mg<sub>2</sub>Zn<sub>3</sub> intermetallic compositions observed using SEM, see Figure 6. Small cracks in the cross-section of all the loose powder HPT disks were observed for equivalent strain higher than 145, see Figure 7 (b). After the equivalent strain became higher than 363, cracks were more widespread throughout the cross-section, see Figure 7 (c).

Table 2. Measurement of the Zn matrix grain sizes for the loose powder HPT disks as a function of the number of turns, equivalent strain, and radius

HPT Turn (N)	Radius (r)	Equivalent strain (ε <sub>eq</sub> )	Grain Size
1	Center	-	3.14 μm
5	Center	-	833 nm
10	Center	-	650 nm
20	Center	-	364 nm
1	2 mm	12	1.57 μm
1	4 mm	24	966 nm
1	4.8 mm	29	1.21 μm
5	4 mm	120	331 nm
5	4.8 mm	145	214 nm

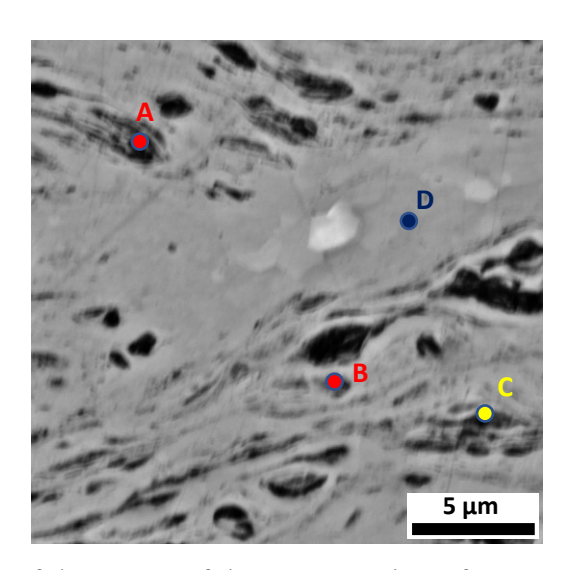


Figure 6. SE-SEM image of the center of the cross-section of Zn-3Mg (wt.%) loose powder HPT disk after 5 turns, where EDS analysis was performed at points A, B, C, and D. Red points show identification of  $Mg_2Zn_3$  intermetallic, the yellow point shows identification of  $Mg_2Zn_{11}$  intermetallic, and the blue point shows Zn matrix phase. Quantitative EDS results are provided in

Table 3. Phase compositions measured at points A, B, C, and D shown in Figure 6 along with those averaged from all the EDS analyzed spots.

	Mg (wt.%)	Zn (wt.%)
Point A*	19.7	80.3
Point B*	20.2	79.8
Point C**	8.6	91.4
Point D (Zn matrix)	2.3	97.7
Zn matrix overall	2.2	97.8
Mg <sub>2</sub> Zn <sub>3</sub> overall	20.1	79.9
Mg <sub>2</sub> Zn <sub>11</sub> overall	7.4	92.6
*Expected composition of Mg <sub>2</sub> Zn <sub>3</sub>	19.86	80.14
**Expected composition of Mg <sub>2</sub> Zn <sub>11</sub>	6.33	93.67

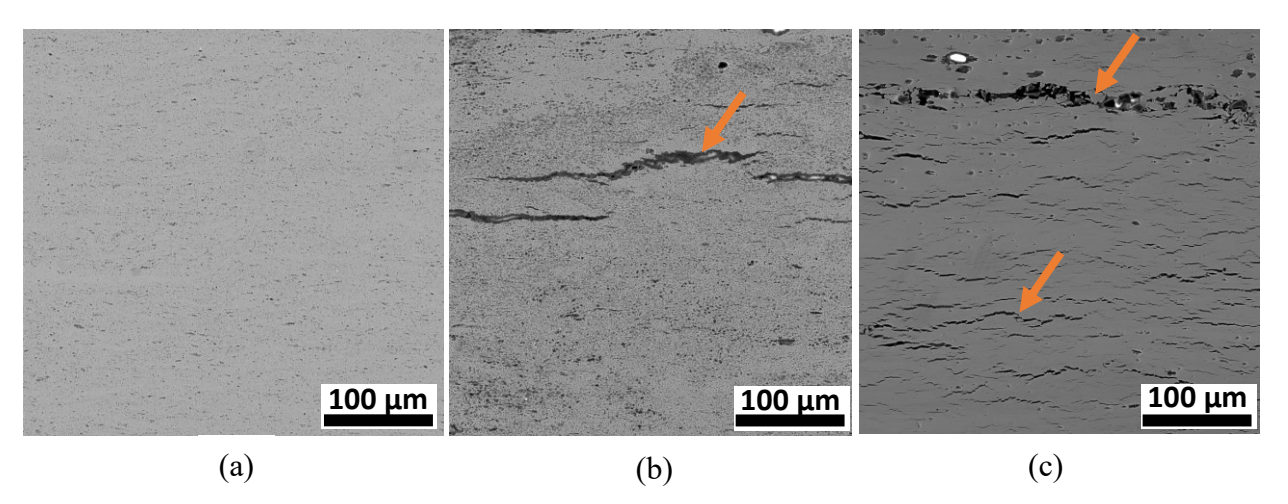


Figure 7. SE-SEM images from the cross-section of Zn-3Mg (wt.%) loose powder HPT disks after a) 5 turns at 2 mm from the center ( $\varepsilon_{eq}$ =60), b) 10 turns at 3 mm from the center ( $\varepsilon_{eq}$ =181), and c) 30 turns at 2 mm from the center ( $\varepsilon_{eq}$ =363). Orange arrows highlight cracks.

Figure 8 shows XRD intensity versus 2θ plots taken from the shear-radial plane at the surface of the loose powder HPT disks, see Figure 2. It is noted that this data represents the entire range of equivalent strains as the XRD spot size resembled that of the disk diameter. To make it easier to resolve the low-intensity peaks from the background, the square root of the intensity is presented on the y-axis. The Zn matrix peaks were larger and more obvious than the ZnO, and Mg<sub>2</sub>Zn<sub>11</sub> and

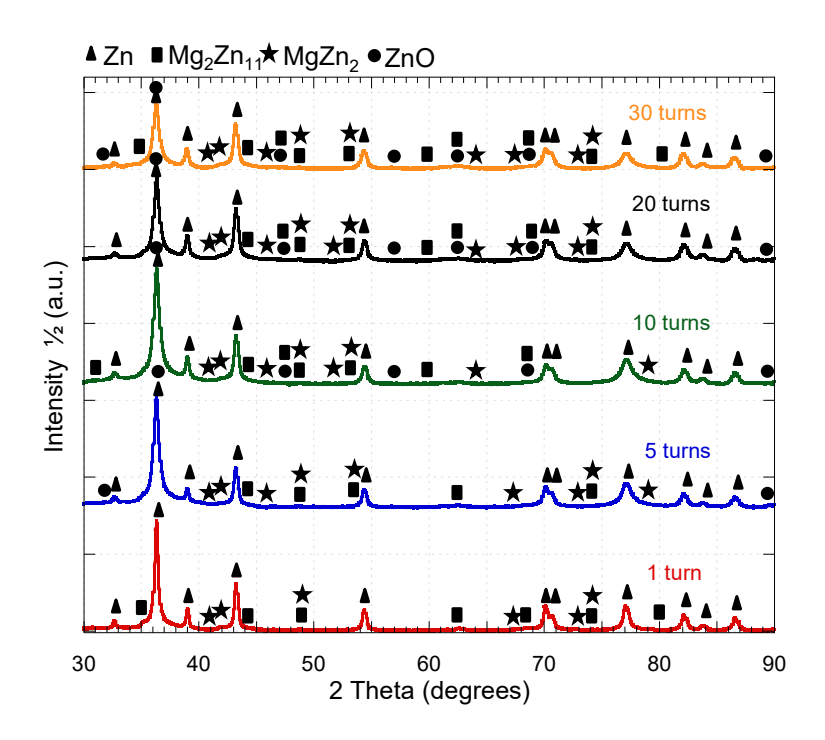


Figure 8. XRD intensity versus 20 plots acquired from the shear-radial plane at the disk surface area of the Zn-3Mg (wt.%) loose powder HPT disks after 1, 5, 10, 20, and 30 turns.

 $MgZn_2$  intermetallic phases suggesting that there was only a small volume fraction of the latter present. It is noted that the  $MgZn_2$  was captured using XRD as the EDS spot analysis did not identify this intermetallic for the loose powder HPT disks.

# 3.2 Microstructural Characterization of the Compact Powder HPT Disks

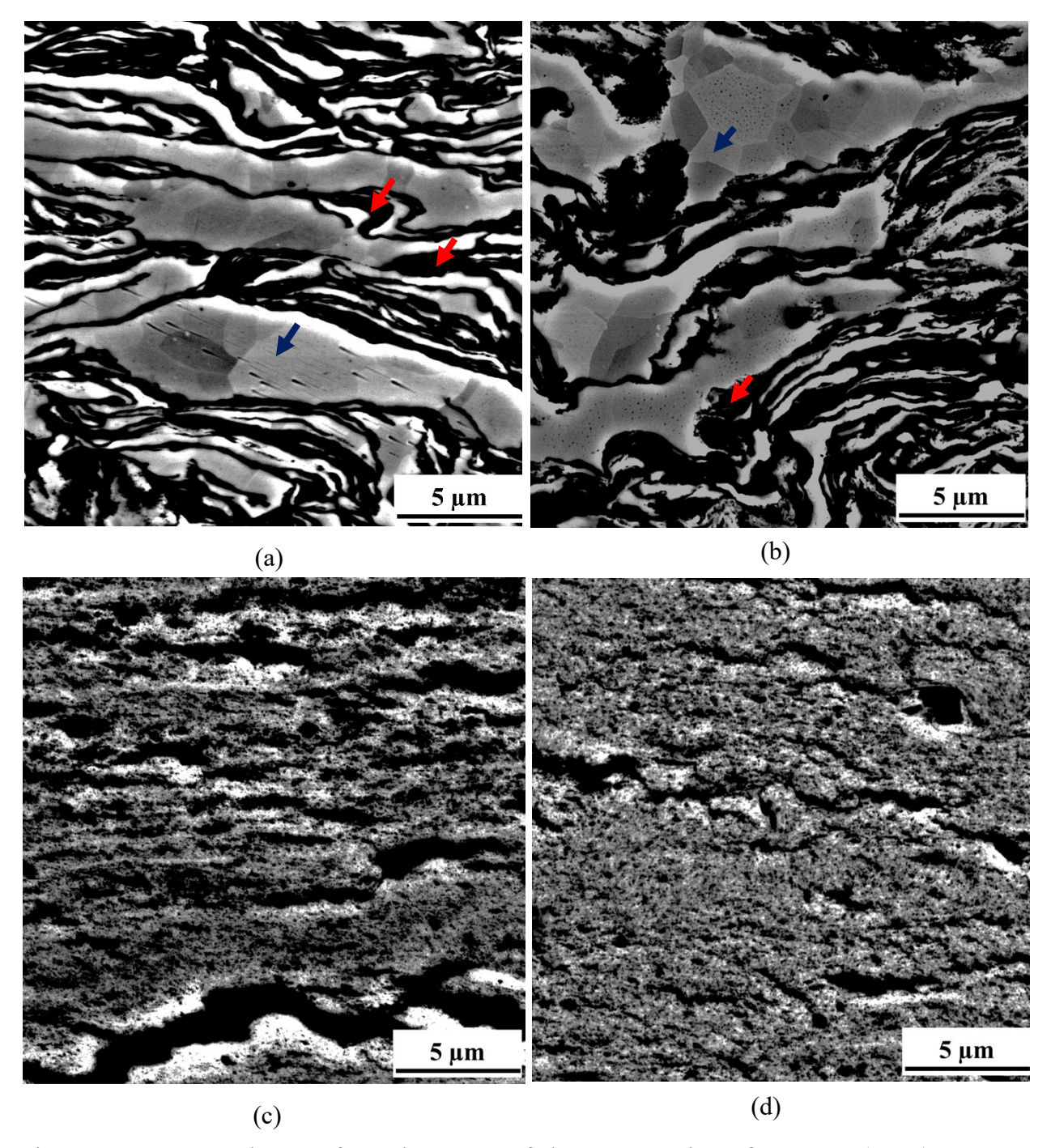


Figure 9. BSE-SEM images from the center of the cross-section of Zn-3Mg (wt.%) compact powder HPT disks after a) 1 turn, b) 5 turns, c) 10 turns, and d) 30 turns at same magnification. Red arrows indicate intermetallic phases and blue arrows indicate ultrafine pure Zn grains.

The compact powder HPT disks exhibited similar microstructures (shown in Figure 9 and Figure 10) compared to those for the loose powder HPT disks (shown in Figure 4 and Figure 5). The Zn

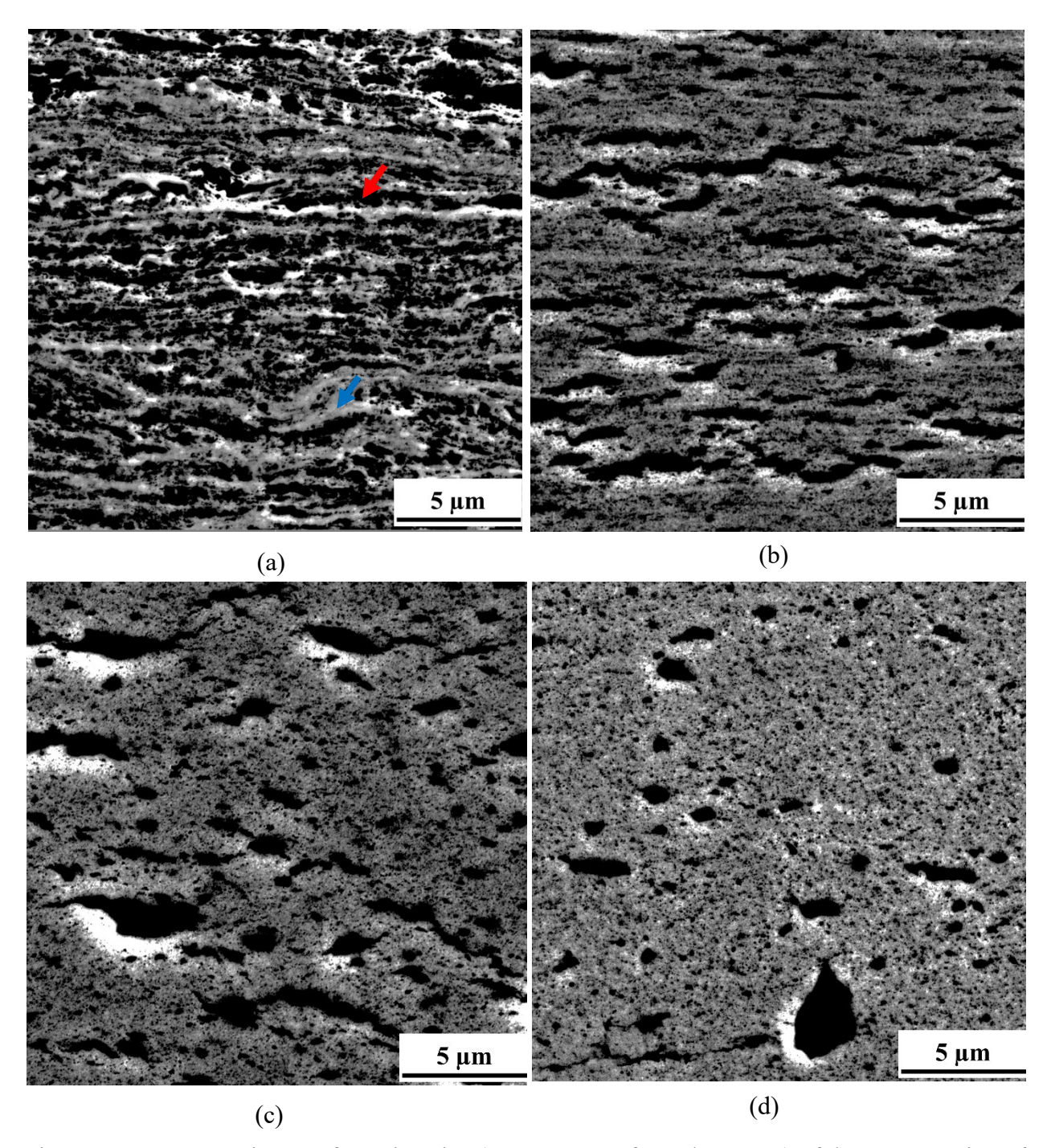


Figure 10. BSE-SEM images from the edge (4.8 mm apart from the center) of the cross-section of Zn-3Mg (wt.%) compact powder HPT disks after a) 1 turn, b) 5 turns, c) 10 turns, and d) 30 turns at same magnification. The red arrow points to the intermetallic phases and the blue arrow points to ultrafine Zn matrix grains.

matrix grain size decreased as the equivalent strain increased. Table 4 summarizes the grain size of the Zn matrix phase, which could not be resolved for equivalent strains greater than 57, as a function of the number of turns, radius, and equivalent strains. Continuous lamellar intermetallic regions of about 2 μm in width (as shown in Figure 9 (a) and (b)) were observed throughout the microstructure for equivalent strains up to about 27. The size of the intermetallic regions decreased to the nano level for greater equivalent strains. Table 5 summarizes the EDS-measured compositions of the Zn matrix and the observed intermetallic phases using SEM, see Figure 11. Small cracks in the cross-section of all the compact powder HPT disks were observed for equivalent strains greater than 57, see Figure 12 (b). For equivalent strains greater than 115, more widespread cracking was observed, see Figure 12 (c).

Table 4. Measurement of the Zn matrix grain sizes of the compact powder HPT disks as a function of the number of turns, equivalent strain, and radius

HPT Turn (N)	Radius (r)	Equivalent strain (ε <sub>eq</sub> )	Grain Size
1	Center	-	3.14 μm
5	Center	-	$2.47~\mu m$
1	2 mm	12	578 nm
1	4 mm	23	388 nm
1	4.8 mm	27	316 nm
5	2	57	223 nm

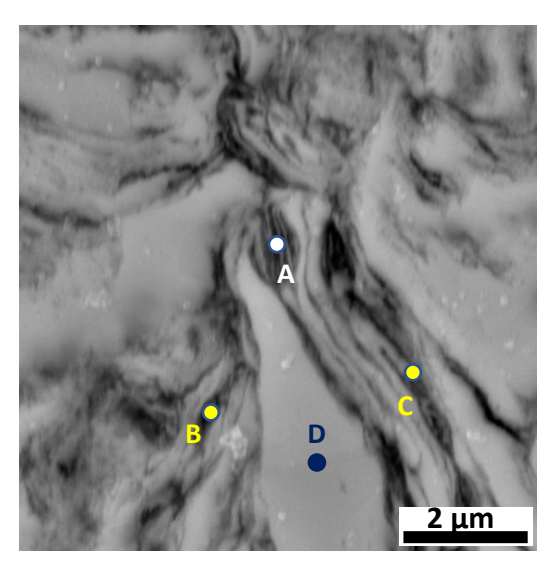


Figure 11. SE-SEM image of the center of the cross-section of Zn-3Mg (wt.%) compact powder HPT disk after 30 turns, where EDS analysis was performed at points A, B, C, and D. The white point indicates the  $MgZn_2$  intermetallic, yellow points indicate the  $Mg_2Zn_{11}$  intermetallic, and the blue point indicates the Zn matrix phase. Quantitative EDS results are provided in Table 5.

Table 5. Phase compositions measured at points A, B, C, and D shown in Figure 11 along with those averaged from all the EDS analyzed spots.

	Mg (wt.%)	Zn (wt.%)
Point A*	12.6	87.4
Point B**	6.9	93.1
Point C**	7.6	92.4
Point D (Zn matrix)	1.5	98.5
Zn matrix overall	2.1	97.9
MgZn <sub>2</sub> overall	13.9	86.1
Mg <sub>2</sub> Zn <sub>11</sub> overall	7.4	92.6
*Expected composition of MgZn <sub>2</sub>	15.67	84.33
**Expected composition of Mg <sub>2</sub> Zn <sub>11</sub>	6.33	93.67

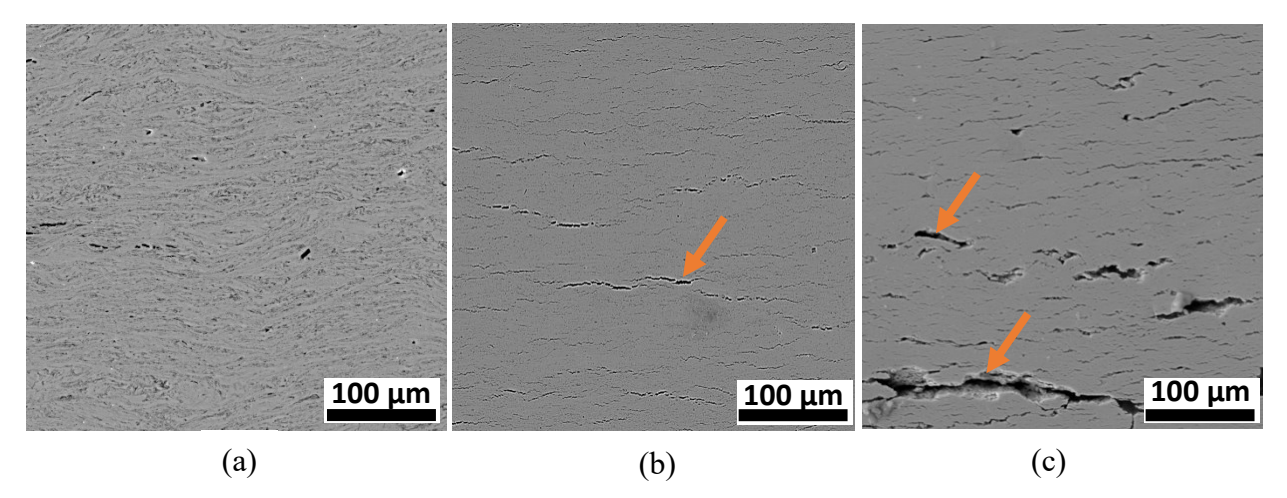


Figure 12. SE-SEM images from the cross-section of Zn-3Mg (wt.%) compact powder HPT disks after a) 1 turn at 2 mm from the center ( $\epsilon_{eq}$ =12), b) 5 turns at 2 mm from the center ( $\epsilon_{eq}$ =57), and c) 10 turns at 2 mm from the center ( $\epsilon_{eq}$ =115). Orange arrows highlight cracks.

Figure 13 shows XRD intensity versus  $2\theta$  plots taken from the shear-radial plane at the surface of the compact powder HPT disks. Similar to that for the loose powder HPT-processed disks, the Zn matrix peaks were larger and more obvious than the intermetallic phases,  $Mg_2Zn_{11}$  and  $MgZn_2$ , and ZnO, suggesting that there was only a small volume fraction of the intermetallic phases and ZnO.

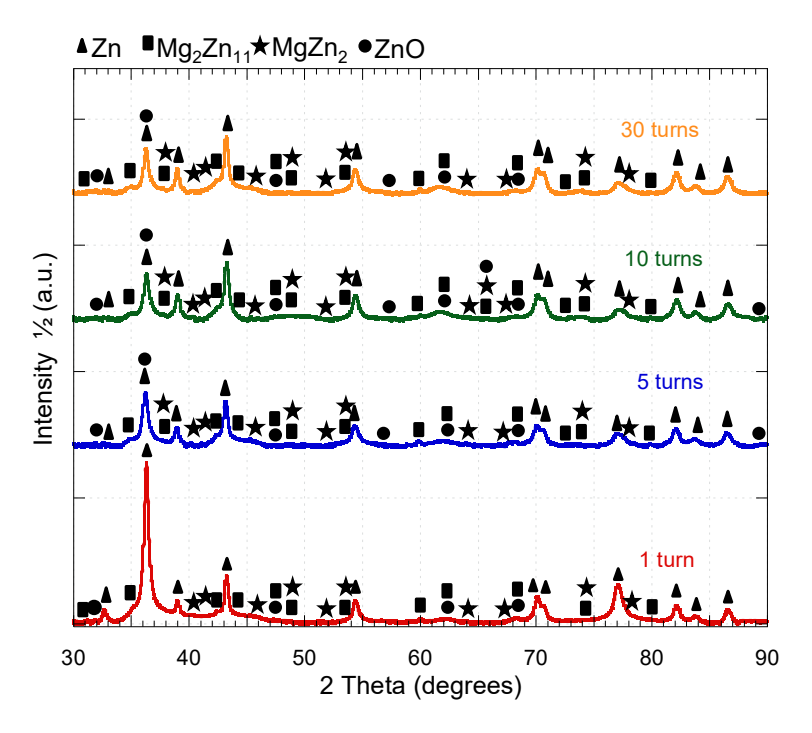


Figure 13. XRD intensity versus 2θ plots acquired from the shear-radial plane at the disk surface area of the Zn-3Mg (wt.%) compact powder HPT disks after 1, 5, 10, and 30 turns.

APT was performed to identify the composition distribution in the local regions of the disks. In particular, this was used to identify the precipitates and their compositions. It is noted that due to the heterogeneous nature of the microstructure, the precipitates were not uniformly distributed and therefore the APT data could not be used to identify the precipitate volume fractions. Figure 14 and Figure 15 present APT atom maps with Mg and O iso-concentration surfaces and their corresponding proximity histograms collected from the cross-section of two different compact powder HPT disks (i.e., 10 turn HPT disk at 4.5 mm distance from the center and 30 turns HPT disk at 1.5 mm distance from the center). Presence of MgZn<sub>2</sub> and ZnO precipitates were evident in Figure 14 (a), and Mg<sub>2</sub>Zn<sub>11</sub> and ZnO precipitates were evident in Figure 15 (a). The black shaded arrow indicates the direction of the corresponding proximity histogram plotted in Figure 14 (b) and Figure 15 (b), which shows the atomic concentration of Zn and Mg as a function of the distance from the isosurface.

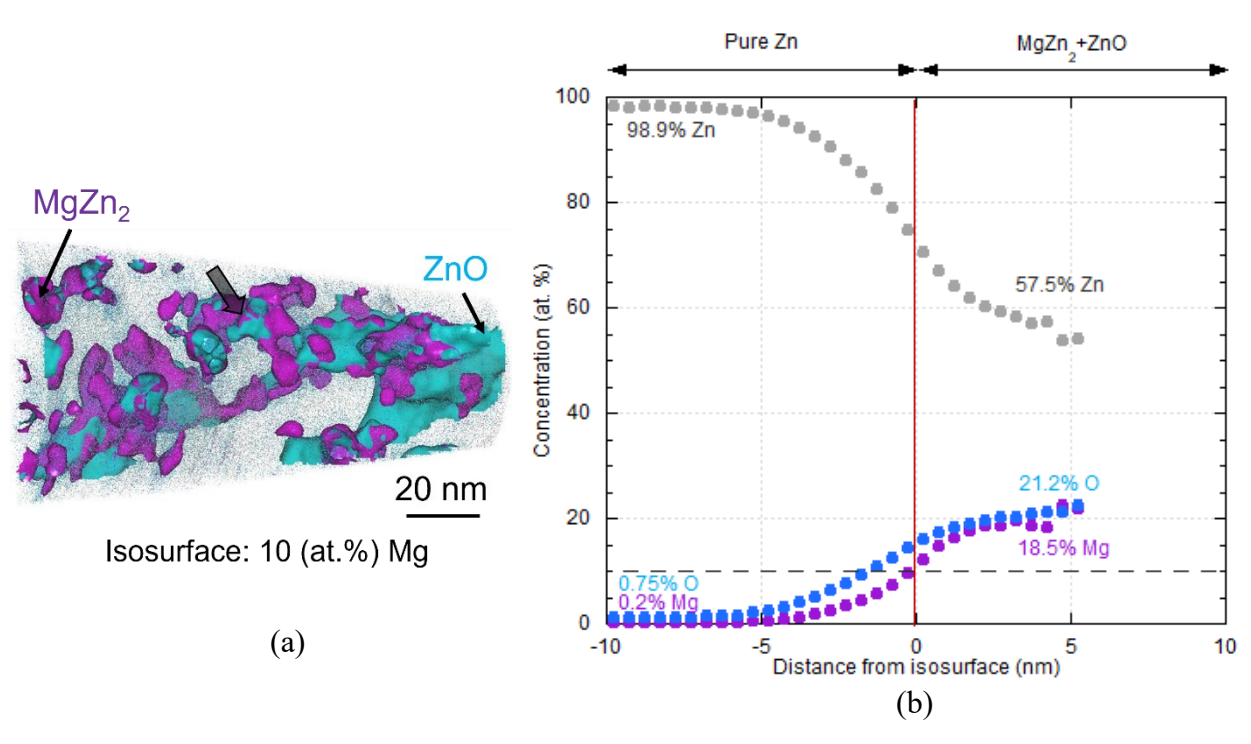


Figure 14. (a) APT reconstruction with O (blue) and Mg (purple) isoconcentration surfaces highlighting ZnO and  $MgZn_2$  particles for compact powder with 10 turns at 4.5 mm distance from the disk center. The open region is the Zn matrix phase. (b) A proximity histogram of the Mg isosurfaces. The black shaded arrow indicates the direction of the corresponding proximity histogram.

It is noted that Mg<sub>2</sub>Zn<sub>11</sub>, MgZn<sub>2</sub> and ZnO phases have overlapping XRD peaks, and therefore they are difficult to uniquely identify in XRD. However, they were distinguished in the APT results. Mg<sub>2</sub>Zn<sub>3</sub> intermetallic was not identified in the two nano-size needles prepared for APT; though it was identified in EDS analysis.

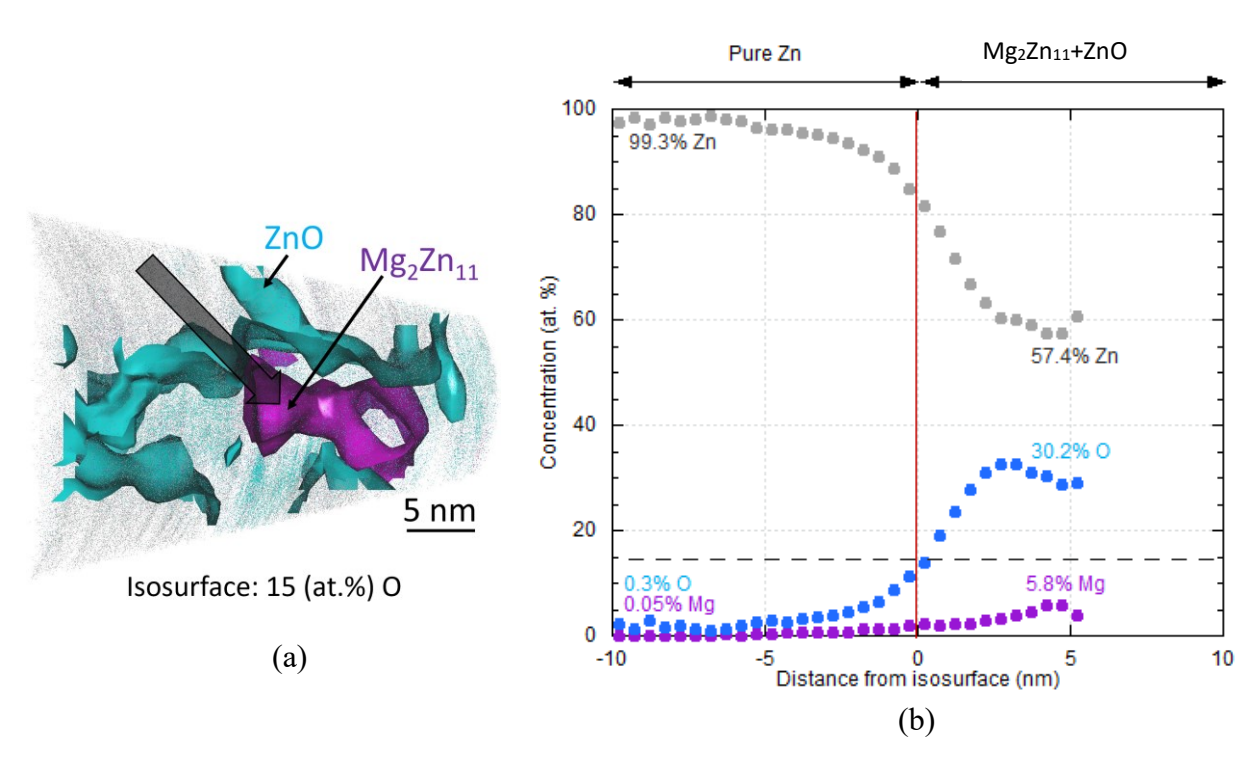


Figure 15. (a) APT reconstruction with O (blue) and Mg (purple) isoconcentration surfaces for compact powder with 30 turns at 1.5 mm distance from the disk center indicating the presence of Mg<sub>2</sub>Zn<sub>11</sub> and ZnO along with the Zn matrix phase. (b) proximity histogram of the O isoconcentration surfaces. The black shaded arrow indicates the direction of the corresponding proximity histogram.

## 3.3 Vickers Hardness Characterization of the Loose and Compact Powder HPT Disks

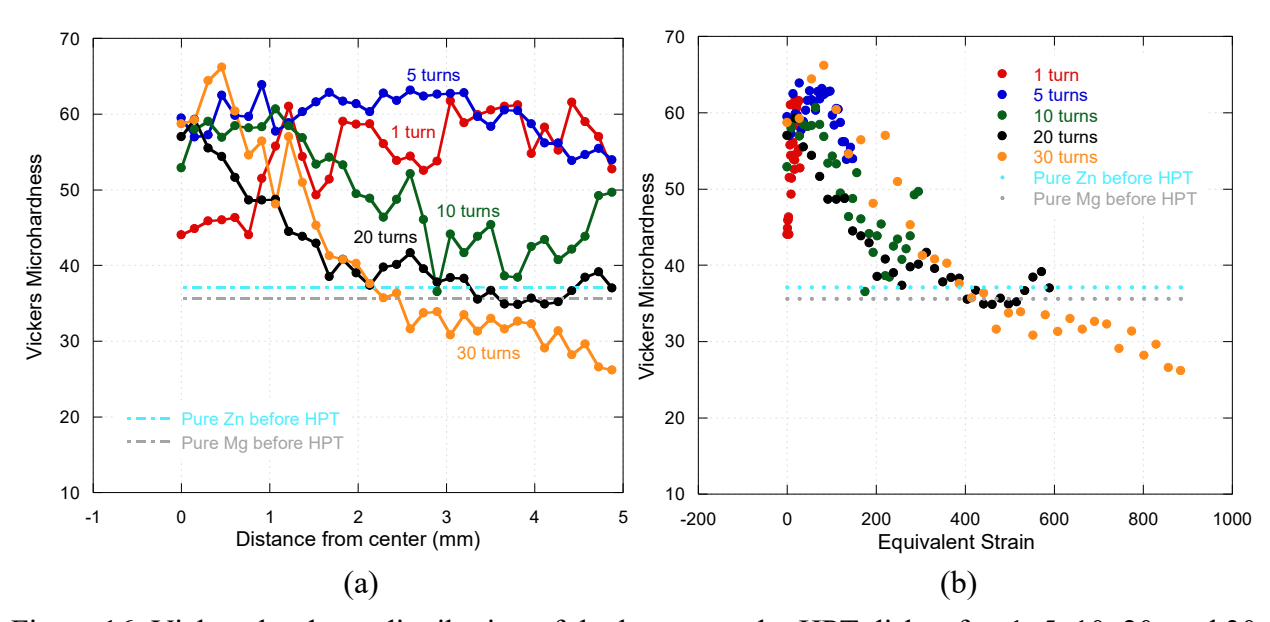


Figure 16. Vickers hardness distribution of the loose powder HPT disks after 1, 5, 10, 20, and 30 turns at the cross-section of the disk as a function of a) distance from the center, and b) equivalent strain.

The Vickers microhardness distribution of the loose powder HPT-processed disks after 1, 5, 10, 20, and 30 turns at the cross-section of the disk as a function of both distances from the center and equivalent strain are provided in Figure 16 (a) and (b), respectively. As discussed in the introduction, the difference in the equivalent strain along the radius of the disks resulted in an inhomogeneous hardness distribution (Figure 16 (a)). However, similar hardness values were measured for similar equivalent strains (Figure 16 (b)). The hardness increased for equivalent strains between 0-80 (max  $\sim$  65 HV) and then decreased thereafter. The hardness values were less than the hardness of cast pure Zn and pure Mg when the equivalent strain was higher than 450 (Figure 16(b)).

The Vickers microhardness distribution of the compact powder HPT disks after 1, 5, 10, and 30 turns at the cross-section of the disk as a function of both distance from the center and equivalent

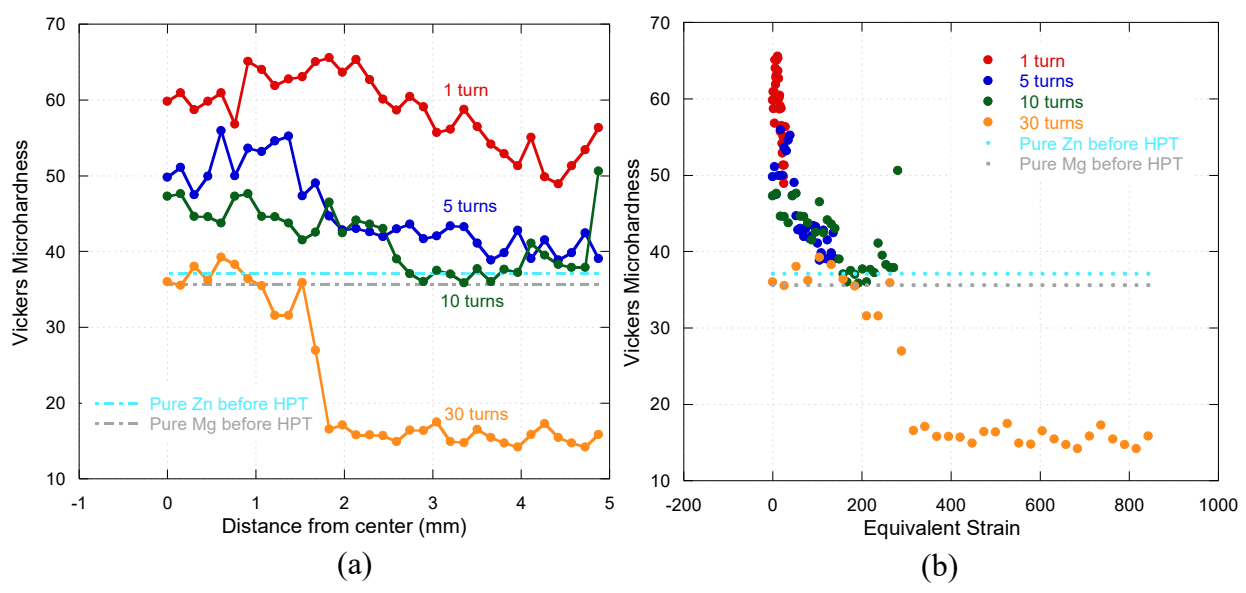


Figure 17. Vickers microhardness distribution of compact powder HPT disks after 1, 5, 10, and 30 turns at the cross-section of the disk as a function of a) distance from the center, and b) equivalent strain.

strain is shown in Figure 17(a) and(b), respectively. Similar to that for the loose powder HPT disks, the compact powder HPT disks showed both an inhomogeneous hardness distribution and similar hardness values for similar equivalent strains, see Figure 17(b). In contrast to the loose powder HPT disks, the hardness values did not increase with either increased distance from the center or equivalent strain. The maximum hardness (~65 HV) was observed close to the center of the disks. The hardness decreased below the hardness of cast pure Zn and cast pure Mg when the equivalent strain was higher than 250 (Figure 17(b)). It is noted that the corresponding value was 450 for the loose powder HPT disks (Figure 16(b)).

#### 4. Discussion

#### 4.1 Microstructure Comparisons of the Loose and Compact Powder HPT Disks

Ultrafine grain microstructures were achieved in the Zn matrix for both the loose and compact powder HPT disks. The combined APT, EDS, and XRD analysis indicated that three different intermetallic phases, Mg<sub>2</sub>Zn<sub>11</sub>, Mg<sub>2</sub>Zn<sub>3</sub>, and MgZn<sub>2</sub>, were present along with the Zn matrix.

Mg<sub>2</sub>Zn<sub>3</sub> intermetallic phase composition was found only in EDS spot analysis. More work, such as TEM characterization, needs to be done to confirm this phase. Figure 18 illustrates the change in the grain size of the Zn matrix as a function of equivalent strain for both the loose and compact powder HPT disks. The Zn matrix grain size decreased from ~3 μm to ~200 nm in both the loose powder (Table 2) and compact powder HPT disks (Table 4) as the equivalent strain increased above 24 and 12 equivalent strain, respectively, see Figure 18. The intermetallic regions also decreased gradually to the nanometer range as the equivalent strain increased. In general, the compact powder HPT disks exhibited a finer grain size than the loose powder HPT disks at any given equivalent strain. This was likely due to the compaction before the processing as the compact would have been more restricted than the loose powders. One study showed that cold pressing of pure Zn powder under 450 MPa (compaction pressure used in this study for the compact powder disks before HPT) is sufficient to start consolidation of the powders [50], whereas the loose powder HPT disks were consolidated during the HPT processing.

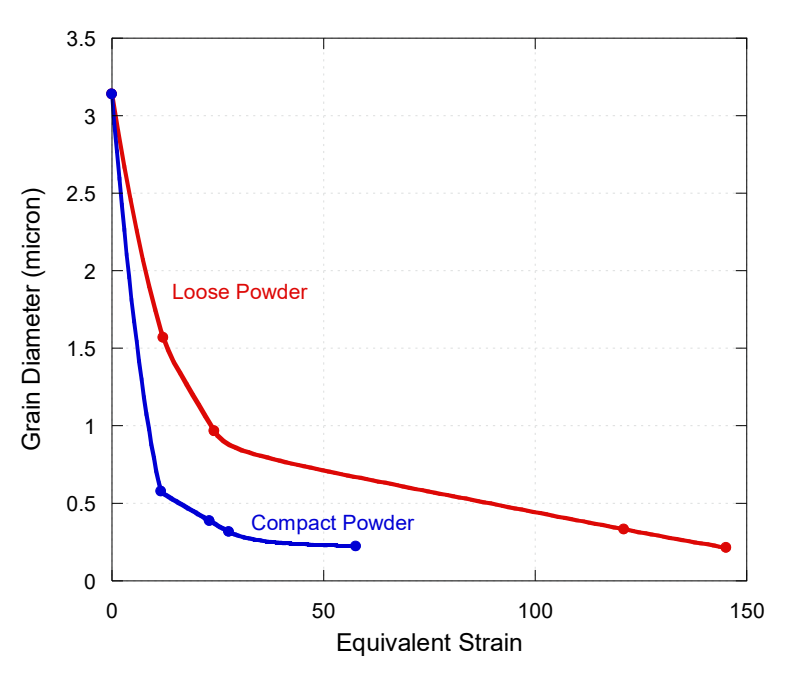


Figure 18. Comparison of the Zn matrix grain size versus equivalent strain for both loose powder and compact powder HPT disks processed through 1 and 5 turns.

Because the compact powder HPT disks were consolidated before HPT processing, it is expected that the compact would realize higher pressure at earlier stages of the HPT processing compared to the loose powder HPT disks. The compact powders could be partially oxidized prior to consolidation and oxide layers might also enhance the grain refinement [51]. The grain sizes of the disks processed in the current work were similar to those of Zn-3Mg (wt.%) HPT-processed alloys and hybrids, where the saturated grain size was ~200 nm [3]. The grain size decreases due to the continuous defect formation and dynamic recrystallization [14], [52].

Mg<sub>2</sub>Zn<sub>11</sub> and MgZn<sub>2</sub> have been observed in Zn-3Mg (wt.%) hybrids and alloys processed by HPT in the study carried out by Hernandez-Escobar et al. [1], [3]. Mg<sub>2</sub>Zn<sub>11</sub> is expected based on the binary phase diagram [53], however, MgZn<sub>2</sub> is considered to be non-equilibrium for Zn-3Mg (wt.%) and therefore is expected to have resulted from the high pressure and torsion experienced during the processing. This is also the case for the Mg<sub>2</sub>Zn<sub>3</sub> phase observed in the EDS data. Formation of non-equilibrium MgZn<sub>2</sub> in HPT-processed Zn-Mg powders and alloys of different compositions was reported in other studies [32], [54], [55] which might be attributed to low Gibbs free energy in the formation of MgZn<sub>2</sub> under high pressure [56], [57].

Hernandez-Escobar et al. did not observe any oxides during the processing of hybrids and alloys through HPT processing [1]–[3]. Thus, the ZnO formed in the current work is unique compared to the literature. Powders tend to result in greater O contents compared to castings due to both the environmental exposure and the high surface areas of the fine powders during processing [51]. This would therefore lead to a higher probability for the formation of oxides in the powder-processed HPT disks compared to the HPT disks processed from cast materials (i.e., those for the HPT processing of castings and hybrids [1]–[3] for example). Even though the standard Gibbs free energy in the formation of MgO is lower than ZnO (-528 kJ vs -278 kJ) [58], application of high

pressure during HPT and higher Zn contents than Mg in the mixture (97 vs 3 wt%) may have influenced the formation of ZnO over MgO. The presence of ZnO in a separate study of HPT-processed Zn and Mg powder by Castro et al. is in agreement with the current observations [32].

Both the loose and compact powder HPT disks exhibited cracking at larger equivalent strains (145 for the loose powder HPT disks and 57 for the compact powder HPT disks). The cracks spread throughout the microstructure at equivalent strains higher than these threshold values. Because the compact powder HPT disks were consolidated before HPT processing, it is expected that the compact powder would realize higher pressure at earlier stages of the HPT processing compared to the loose powder HPT disks, as described above in the discussion regarding the different equivalent strains required to reach the grain size saturation level. This would likely result in the formation of the intermetallic phases and ZnO at an earlier strain than for the loose powder HPT disks. This would therefore explain why cracking was observed at lower equivalent strains in the compact powder HPT disks compared to the loose powder HPT-processed disks. The density measurement data provided in Table 1, which shows that the density decreases with the increasing number of turns, is in agreement with the cracking observed with the increased number of turns in the current work.

It is noted that cracking was not observed in Zn-3Mg (wt.%) alloys and hybrids [1], [3]. It is expected that the larger O contents in the powders likely lead to cracking. It is well known that the oxides tend to exhibit less slip propensity than metallic solid solutions and therefore are more likely to exhibit a brittle response during deformation.

# 4.2 Comparisons of the Hardness Distributions of the Loose Powder and Compact HPT Disks

The maximum hardness value of both the loose and compact powder HPT disks was identical (~65 HV). The maximum hardness was achieved at a higher equivalent strain in the loose powder HPT disks (Figure 16(b)) than for the compact powder HPT disks (Figure 17(b)). This was likely due to the compaction prior to the HPT processing as discussed above. The compaction and subsequent earlier grain refinement are expected to have led to the maximum hardness being achieved at a lower equivalent strain for the compact powder HPT disks. The maximum hardness achieved in the current HPT disks was significantly lower than the maximum hardness values achieved in alloy-processed HPT disks and hybrids of the same composition [1], [3]. Figure 19 compares the hardness distributions of the current materials with those for the cast HPT alloys and hybrids after 30 turns from Hernadez-Escobar et al. [1], [3]. This plot shows the limited increase in hardness capable through HPT processing of powder forms. It is believed that the larger volume fractions

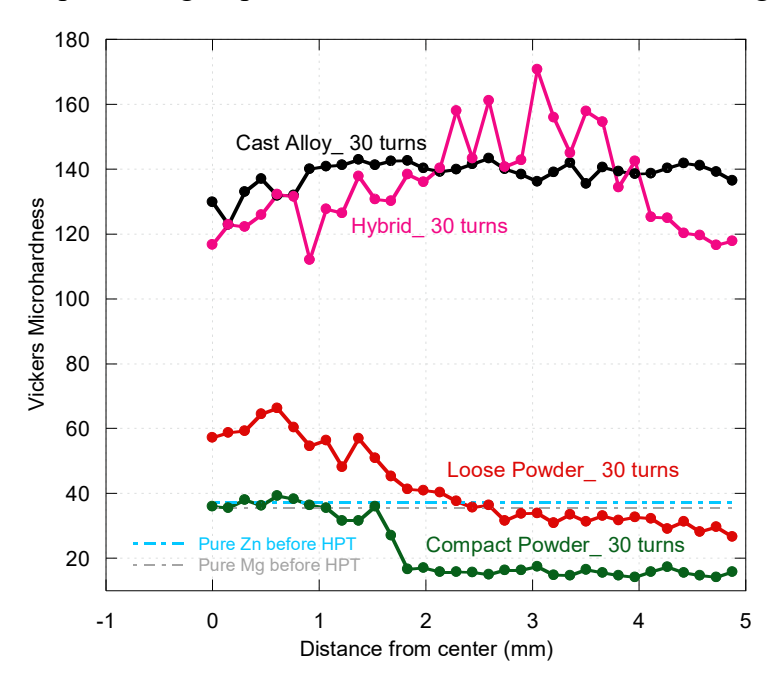


Figure 19. Comparison of Vickers microhardness distribution of different types of Zn-3Mg (wt.%) HPT disks after 30 turns [1], [3].

of the intermetallic phases would result in increased hardness values for alloy and hybrid HPT disks as indicated by the high-intensity XRD peaks from the intermetallics in [1]. The intermetallic phase volume fraction was small for the current samples as indicated by the XRD data, see Figure 8 and Figure 13. Thus, one reason why the powder HPT-processed Zn-3Mg (wt.%) disks in the current work did not achieve the high hardness values in comparison to the HPT-processed cast alloys and hybrids of the same composition [1], [3] was due to the lower amounts of intermetallic compounds that formed. The grain sizes of the HPT-processed cast alloys and hybrids and powders were similar, where the steady-state grain sizes were around 200 nm. Therefore, the same contributions to hardening from the grain size refinement would be expected for all the cases.

It is noted that the maximum hardness values of the powder HPT disks in the current work were greater than those for cast pure Zn (max ~50 HV) [5] and pure Mg (max ~40 HV) [59]. The hardness decreased with increased equivalent strain after maximum hardness was achieved in both the loose and compact powder HPT disks despite their grain refinement, see Figure 16(b), Figure 17(b), and Figure 18. It should be noted that softening by straining observed in this study was reported for pure Zn [5] and Mg [59] as well. It was shown by Figueiredo et al. using creep analysis that such a softening can happen for metals having low melting points due to the occurrence of grain boundary sliding at room temperature [60]. Zn and Mg both are considered to have low melting points (420 °C and 650 °C for Zn and Mg, respectively) [5]. A similar mechanism likely occurs in the Zn matrix phase of the current Zn-3Mg (wt.%) HPT disks, despite the formation of some intermetallics. This inverse Hall-Petch relationship between hardness and grain size is an indication that room-temperature grain boundary sliding should contribute to unusual strain softening of these nano-structured materials in this study. It is noted that softening at higher equivalent strain was not observed in HPT-processed cast alloys and hybrids [1], [3] due to the

presence of higher volume fraction of intermetallic compounds than the current study. Current results suggest that nanograin formation is not necessarily a solution to enhance the strength of biodegradable Zn-Mg alloys for biomedical applications. In addition, based on the current observations, the generation of cracks and oxidation due to HPT processing of the powders also have detrimental effects and may limit the strengthening, ductility and fracture toughness of the disks.

## 4.3 Steady-State Behavior

Edalati et al. showed that different hardness responses as a function of equivalent strain exist for different materials [5]. Despite the microstructural evolution and phase transitions in the early stages of straining, the microstructural features become saturated at large strain, where a steadystate is achieved and the hardness values remain relatively constant [14], [16]. The different profiles for the hardness distribution as a function of equivalent strain and radial distance from the center of the disk have been related to their homologous temperature [5], [17]. In the cases where increased hardness correlated with increased equivalent strain (up to a maximum level where thereafter a plateau, or steady-state, was achieved) [4], [5], [14], no or little recovery was experienced in the materials during the early straining stages of HPT processing. This is because the recombination of the partial dislocations necessary to cross-slip is difficult, particularly for materials with high melting point and low stacking fault energy (SFE) [61]. In materials with higher homologous temperature and lower melting point, a maximum hardness was achieved at a certain equivalent strain, and with increased equivalent strain thereafter a decrease in the hardness was observed until a steady-state hardness was achieved [4], [5], [14]. In such materials, recovery is experienced during the early stage of HPT processing, as the recombination of the partial dislocations necessary to cross-slip is easier [61]. The latter occurred in the loose powder HPT disks, see Figure 16(b), which exhibited hardness behavior similar to that for pure Zn [5] and Mg [59].

Zn and Mg both are considered to have low melting points and exhibit relatively high SFE (140 mJm<sup>-2</sup> and 125 mJm<sup>-2</sup> for Zn and Mg, respectively) [5]. The hardness of the compact powder HPT disks decreased from zero equivalent strain (Figure 17(b)), which might be because the hardness reached the maximum close to the center of the disks due to compaction before HPT. The loose powder HPT disks attained the steady-state at an equivalent strain of approximately 250 whereas the compact powder HPT disks likely attained the steady-state at an equivalent strain of approximately 175, earlier than the loose powder HPT disks. This is likely due to the early consolidation of the compact powder HPT disks resulting in smaller Zn matrix grain sizes at similar equivalent strains compared to the loose powder HPT disks as previously discussed. It is noted that the steady-state hardness level in the current disks was likely to have been affected by cracking, where the cracking resulted in continued decreases in the hardness values.

Zhang et al. studied a cast Zn-22Al (wt.%) alloy that was subsequently HPT-processed, and the hardness decreased with an increased equivalent strain before reaching the steady-state even though grain size decreased to nanometer scales [62]. The reason for this behavior was attributed to the absorption of Zn precipitates due to intense plastic straining. A similar hardness distribution was found for the Pb-62Sn (wt.%) alloy [62]. It is to be noted that both alloys exhibit a eutectic where the two pure metal phases are possibly miscible, and no intermetallic phases were present in the microstructure. In another study, an HPT-processed Al-33Cu (wt.%) eutectic alloy exhibited an increase of hardness before reaching a steady-state hardness level and intermetallic particles were present in the microstructure (i.e., a multiphase microstructure with immiscible phases) [63]. The current study involved different intermetallic particles in the microstructure which explains

the hardness increase before reaching the steady-state for a multiphase material with immiscible phases. This suggests that in addition to the homologous temperature and SFE, the presence of immiscible ordered intermetallic phases may also influence the steady-state behavior of multiphase materials.

#### 5. Summary and Conclusions

HPT was carried out on mixture of pure Zn and Mg powders, according to the targeted Zn-3Mg (wt.%) composition, to study the microstructural evolution, multiphase formation, and hardness distribution. In order to understand the effects of pre-consolidation on the resulting microstructure and hardness of this biomaterial, HPT processing was performed on loose powders placed in the die and also on a compact, where the powders were first pressed together prior to HPT processing. The following conclusions were obtained.

- 1. HPT resulted in the refinement of the Zn matrix grains in both the loose powder and compact powder disks, where the compact powder HPT disks exhibited finer grain sizes than the loose powder HPT disks at identical equivalent strains.
- 2. The formation of Mg<sub>2</sub>Zn<sub>11</sub>, Mg<sub>2</sub>Zn<sub>3</sub>, and MgZn<sub>2</sub> intermetallics and ZnO were observed in the HPT disks. The intermetallics decreased in size with increased equivalent strain. Cracking was exhibited in the samples once a respective threshold equivalent strain was achieved for both the loose and compact powder HPT disks.
- 3. The hardness evolution of the different disks was consistent as similar hardness values were measured for similar equivalent strains. Softening occurred at large equivalent strains in both the loose and compact powder HPT disks. The compact powder HPT disks attained the maximum hardness at a lower equivalent strain than the loose powder HPT disks due to the early

consolidation of the compact powder HPT disks, which resulted in smaller Zn matrix grain sizes at similar equivalent strains.

4.HPT-processed Zn-3Mg cast alloys and hybrids resulted in larger hardness values than those for the current work and one reason for this was because of the larger volume of intermetallic compounds present in that study.

5. The presence of immiscible ordered intermetallic phases influenced the hardness distribution (i.e., the steady-state behavior) of the HPT-processed disks.

Overall, this study suggests that nanoscale grain refinement may not be a solution to enhance the hardness of Zn-Mg biodegradable alloys due to the contribution of thermally-activated phenomena such as grain boundary sliding.

# **CRediT** authorship contribution statement

Tanzilur Rahman: Conceptualization, Methodology, Investigation, Data analysis, Writing – original draft, Data curation. Hakan Yilmazer: Methodology, Investigation, Writing – review & editing. Burak Dikici: Methodology, Investigation, Writing – review & editing. Kaveh Edalati: Methodology, Investigation, Writing – review & editing. Jonathan D. Poplawsky: Investigation, Writing – review & editing. Carl J. Boehlert: Conceptualization, Writing – review & editing, Supervision, Project administration, Funding acquisition.

#### **Declaration of competing interest**

The authors declare that they have no known competing financial interests or personal relationships that could have appeared to influence the work reported in this paper.

#### Acknowledgments

The authors would also like to acknowledge Dr. Per Askeland of Michigan State University for his helpful discussions and technical assistance. APT research was supported by the Center for Nanophase Materials Sciences (CNMS), which is a US Department of Energy, Office of Science User Facility at Oak Ridge National Laboratory. The authors would like to thank James Burns for assistance in performing APT sample preparation and running the APT experiments. A portion of the funding for this research was provided by the National Science Foundation Division of Materials Research (Grant No. DMR 1607942) through the Metals and Metallic Nanostructures, and the National Science Foundation Division of Engineering (Grant No. 2148646) through the Civil, Mechanical and Manufacturing Innovation Program.

#### Data availability

Data will be made available on request.

#### References

- [1] D. Hernández-Escobar, J. Marcus, J.-K. Han, R. R. Unocic, M. Kawasaki, and C. J. Boehlert, "Effect of post-deformation annealing on the microstructure and micro-mechanical behavior of Zn–Mg hybrids processed by High-Pressure Torsion," *Mater. Sci. Eng. A*, vol. 771, p. 138578, Jan. 2020, doi: 10.1016/j.msea.2019.138578.
- [2] D. Hernández-Escobar, Z. U. Rahman, H. Yilmazer, M. Kawasaki, and C. J. Boehlert, "Microstructural evolution and intermetallic formation in Zn-Mg hybrids processed by High-Pressure Torsion," *Philos. Mag.*, vol. 99, no. 5, pp. 557–584, Mar. 2019, doi: 10.1080/14786435.2018.1546962.
- [3] D. Hernández-Escobar, R. R. Unocic, M. Kawasaki, and C. J. Boehlert, "High-pressure torsion processing of Zn–3Mg alloy and its hybrid counterpart: A comparative study," *J. Alloys Compd.*, vol. 831, p. 154891, Aug. 2020, doi: 10.1016/j.jallcom.2020.154891.
- [4] M. Kawasaki, "Different models of hardness evolution in ultrafine-grained materials processed by high-pressure torsion," *J. Mater. Sci.*, vol. 49, no. 1, pp. 18–34, Jan. 2014, doi: 10.1007/s10853-013-7687-9.
- [5] K. Edalati and Z. Horita, "Significance of homologous temperature in softening behavior and grain size of pure metals processed by high-pressure torsion," *Mater. Sci. Eng. A*, vol. 528, no. 25, pp. 7514–7523, Sep. 2011, doi: 10.1016/j.msea.2011.06.080.

- [6] K. Edalati, Y. Hashiguchi, P. H. R. Pereira, Z. Horita, and T. G. Langdon, "Effect of temperature rise on microstructural evolution during high-pressure torsion," *Mater. Sci. Eng. A*, vol. 714, pp. 167–171, Jan. 2018, doi: 10.1016/j.msea.2017.12.095.
- [7] B. Straumal, A. Korneva, and P. Zieęba, "Phase transitions in metallic alloys driven by the high pressure torsion," *Arch. Civ. Mech. Eng.*, vol. 14, no. 2, pp. 242–249, Jun. 2014, doi: 10.1016/j.acme.2013.07.002.
- [8] B. B. Straumal *et al.*, "Phase transitions in Cu-based alloys under high pressure torsion," *J. Alloys Compd.*, vol. 707, pp. 20–26, Jun. 2017, doi: 10.1016/j.jallcom.2016.12.057.
- [9] A. R. Kilmametov *et al.*, "The  $\alpha \rightarrow \omega$  and  $\beta \rightarrow \omega$  phase transformations in Ti–Fe alloys under high-pressure torsion," *Acta Mater.*, vol. 144, pp. 337–351, Feb. 2018, doi: 10.1016/j.actamat.2017.10.051.
- [10] P. F. Yu *et al.*, "Effects of high pressure torsion on microstructures and properties of an Al0.1CoCrFeNi high-entropy alloy," *Mater. Sci. Eng. A*, vol. 655, pp. 283–291, Feb. 2016, doi: 10.1016/j.msea.2015.12.085.
- [11] F. A. Mohamed and S. S. Dheda, "On the minimum grain size obtainable by high-pressure torsion," *Mater. Sci. Eng. A*, vol. 558, pp. 59–63, Dec. 2012, doi: 10.1016/j.msea.2012.07.066.
- [12] V. N. Danilenko *et al.*, "An approach for fabrication of Al-Cu composite by high pressure torsion," *Mater. Lett.*, vol. 236, pp. 51–55, Feb. 2019, doi: 10.1016/j.matlet.2018.09.158.
- [13] D. Hernández-Escobar, M. Kawasaki, and C. J. Boehlert, "Metal hybrids processed by high-pressure torsion: synthesis, microstructure, mechanical properties and developing trends," *Int. Mater. Rev.*, vol. 67, no. 3, pp. 231–265, Apr. 2022, doi: 10.1080/09506608.2021.1922807.
- [14] K. Edalati and Z. Horita, "A review on high-pressure torsion (HPT) from 1935 to 1988," *Mater. Sci. Eng. A*, vol. 652, pp. 325–352, Jan. 2016, doi: 10.1016/j.msea.2015.11.074.
- [15] A. P. Zhilyaev and T. G. Langdon, "Using high-pressure torsion for metal processing: Fundamentals and applications," *Prog. Mater. Sci.*, vol. 53, no. 6, pp. 893–979, Aug. 2008, doi: 10.1016/j.pmatsci.2008.03.002.
- [16] R. Pippan, S. Scheriau, A. Taylor, M. Hafok, A. Hohenwarter, and A. Bachmaier, "Saturation of Fragmentation During Severe Plastic Deformation," *Annu. Rev. Mater. Res.*, vol. 40, no. 1, pp. 319–343, 2010, doi: 10.1146/annurev-matsci-070909-104445.
- [17] K. Edalati and Z. Horita, "High-pressure torsion of pure metals: Influence of atomic bond parameters and stacking fault energy on grain size and correlation with hardness," *Acta Mater.*, vol. 59, no. 17, pp. 6831–6836, Oct. 2011, doi: 10.1016/j.actamat.2011.07.046.
- [18] M. J. Starink, X. Cheng, and S. Yang, "Hardening of pure metals by high-pressure torsion: A physically based model employing volume-averaged defect evolutions," *Acta Mater.*, vol. 61, no. 1, pp. 183–192, Jan. 2013, doi: 10.1016/j.actamat.2012.09.048.
- [19] T. Sakai, A. Belyakov, R. Kaibyshev, H. Miura, and J. J. Jonas, "Dynamic and post-dynamic recrystallization under hot, cold and severe plastic deformation conditions," *Prog. Mater. Sci.*, vol. 60, no. 1, pp. 130–207, 2014, doi: 10.1016/j.pmatsci.2013.09.002.
- [20] A. Mishra, B. K. Kad, F. Gregori, and M. A. Meyers, "Microstructural evolution in copper subjected to severe plastic deformation: Experiments and analysis," *Acta Mater.*, vol. 55, no. 1, pp. 13–28, Jan. 2007, doi: 10.1016/j.actamat.2006.07.008.
- [21] X. Sauvage, F. Wetscher, and P. Pareige, "Mechanical alloying of Cu and Fe induced by severe plastic deformation of a Cu–Fe composite," *Acta Mater.*, vol. 53, no. 7, pp. 2127–2135, Apr. 2005, doi: 10.1016/j.actamat.2005.01.024.

- [22] Yu. Ivanisenko, I. MacLaren, X. Sauvage, R. Z. Valiev, and H.-J. Fecht, "Shear-induced α→γ transformation in nanoscale Fe–C composite," *Acta Mater.*, vol. 54, no. 6, pp. 1659–1669, Apr. 2006, doi: 10.1016/j.actamat.2005.11.034.
- [23] K. S. Kormout, R. Pippan, and A. Bachmaier, "Deformation-Induced Supersaturation in Immiscible Material Systems during High-Pressure Torsion," *Adv. Eng. Mater.*, vol. 19, no. 4, p. 1600675, 2017, doi: 10.1002/adem.201600675.
- [24] K. Edalati *et al.*, "Ultra-severe plastic deformation: Evolution of microstructure, phase transformation and hardness in immiscible magnesium-based systems," *Mater. Sci. Eng. A*, vol. 701, pp. 158–166, Jul. 2017, doi: 10.1016/j.msea.2017.06.076.
- [25] E. Y. Yoon, D. J. Lee, D.-H. Ahn, E. S. Lee, and H. S. Kim, "Mechanical properties and thermal stability of bulk Cu cold consolidated from atomized powders by high-pressure torsion," *J. Mater. Sci.*, vol. 47, no. 22, pp. 7770–7776, Nov. 2012, doi: 10.1007/s10853-012-6569-x.
- [26] A. P. Zhilyaev, G. Ringot, Y. Huang, J. Maria Cabrera, and T. G. Langdon, "Mechanical behavior and microstructure properties of titanium powder consolidated by high-pressure torsion," *Mater. Sci. Eng. A*, vol. 688, pp. 498–504, Mar. 2017, doi: 10.1016/j.msea.2017.02.032.
- [27] R. Z. Valiev, R. S. Mishral, J. Grozal, and A. K. Mukherjee, "Processing of nano-structured nickel by severe plastic deformation consolidation of ball-milled powder," *Scr. Mater.*, vol. 34, no. 9, pp. 1443–1448, May 1996, doi: 10.1016/1359-6462(95)00676-1.
- [28] S. Panda, J.-J. Fundenberger, Y. Zhao, J. Zou, L. S. Toth, and T. Grosdidier, "Effect of initial powder type on the hydrogen storage properties of high-pressure torsion consolidated Mg," *Int. J. Hydrog. Energy*, vol. 42, no. 35, pp. 22438–22448, Aug. 2017, doi: 10.1016/j.ijhydene.2017.05.097.
- [29] C. Borchers *et al.*, "Nanocrystalline steel obtained by mechanical alloying of iron and graphite subsequently compacted by high-pressure torsion," *Acta Mater.*, vol. 97, pp. 207–215, Sep. 2015, doi: 10.1016/j.actamat.2015.06.049.
- [30] H. Shen, Z. Li, B. Günther, A. V. Korznikov, and R. Z. Valiev, "Influence of powder consolidation methods on the structural and thermal properties of a nanophase Cu-50wt%Ag alloy," *Nano-structured Mater.*, vol. 6, no. 1, pp. 385–388, Jan. 1995, doi: 10.1016/0965-9773(95)00077-1.
- [31] Z. Lee, F. Zhou, R. Z. Valiev, E. J. Lavernia, and S. R. Nutt, "Microstructure and microhardness of cryomilled bulk nanocrystalline Al–7.5%Mg alloy consolidated by high pressure torsion," *Scr. Mater.*, vol. 51, no. 3, pp. 209–214, Aug. 2004, doi: 10.1016/j.scriptamat.2004.04.016.
- [32] M. M. Castro, L. A. Montoro, A. Isaac, M. Kawasaki, and R. B. Figueiredo, "Mechanical mixing of Mg and Zn using high-pressure torsion," *J. Alloys Compd.*, vol. 869, p. 159302, Jul. 2021, doi: 10.1016/j.jallcom.2021.159302.
- [33] K. Edalati, Y. Yokoyama, and Z. Horita, "High-Pressure Torsion of Machining Chips and Bulk Discs of Amorphous Zr<SUB>50</SUB>Cu<SUB>30</SUB>Al<SUB>10</SUB>Ni<SUB>10</SUB>," *Mater. Trans.*, vol. advpub, pp. 0911300948–0911300948, 2010, doi: 10.2320/matertrans.MB200914.
- [34] K. Edalati and Z. Horita, "Application of high-pressure torsion for consolidation of ceramic powders," *Scr. Mater.*, vol. 63, no. 2, pp. 174–177, Jul. 2010, doi: 10.1016/j.scriptamat.2010.03.048.

- [35] E. Menéndez *et al.*, "Cold compaction of metal–ceramic (ferromagnetic–antiferromagnetic) composites using high pressure torsion," *J. Alloys Compd.*, vol. 434–435, pp. 505–508, May 2007, doi: 10.1016/j.jallcom.2006.08.142.
- [36] E. Menéndez *et al.*, "Cold Consolidation of Metal–Ceramic Nanocomposite Powders with Large Ceramic Fractions," *Adv. Funct. Mater.*, vol. 18, no. 20, pp. 3293–3298, 2008, doi: 10.1002/adfm.200800456.
- [37] K. Edalati, "Review on Recent Advancements in Severe Plastic Deformation of Oxides by High-Pressure Torsion (HPT)," *Adv. Eng. Mater.*, vol. 21, no. 1, p. 1800272, 2019, doi: 10.1002/adem.201800272.
- [38] S. Son, P. Asghari-Rad, A. Zargaran, W. Chen, and H. S. Kim, "Superlative room temperature and cryogenic tensile properties of nano-structured CoCrFeNi medium-entropy alloy fabricated by powder high-pressure torsion," *Scr. Mater.*, vol. 213, p. 114631, May 2022, doi: 10.1016/j.scriptamat.2022.114631.
- [39] K. Edalati, H.-W. Li, A. Kilmametov, R. Floriano, and C. Borchers, "High-Pressure Torsion for Synthesis of High-Entropy Alloys," *Metals*, vol. 11, no. 8, Art. no. 8, Aug. 2021, doi: 10.3390/met11081263.
- [40] A. Kilmametov *et al.*, "High-pressure torsion driven mechanical alloying of CoCrFeMnNi high entropy alloy," *Scr. Mater.*, vol. 158, pp. 29–33, Jan. 2019, doi: 10.1016/j.scriptamat.2018.08.031.
- [41] M. A. Maruf, M. Noor-A-Alam, W. Haider, and I. Shabib, "Enhancing controlled and uniform degradation of Fe by incorporating Mg and Zn aimed for bio-degradable material applications," *Mater. Chem. Phys.*, vol. 285, p. 126171, Jun. 2022, doi: 10.1016/j.matchemphys.2022.126171.
- [42] D. Hernández Escobar and this link will open in a new window Link to external site, "Composition Processing Microstructure Property Relationships of the Zinc-Magnesium System for Absorbable Biomedical Implant Applications," Ph.D., Michigan State University, United States -- Michigan, 2021. Accessed: Nov. 08, 2022. [Online]. Available: https://www.proquest.com/docview/2529227234/abstract/918CF81923042EBPQ/3
- [43] C. Yao, Z. Wang, S. L. Tay, T. Zhu, and W. Gao, "Effects of Mg on microstructure and corrosion properties of Zn–Mg alloy," *J. Alloys Compd.*, vol. 602, pp. 101–107, Jul. 2014, doi: 10.1016/j.jallcom.2014.03.025.
- [44] "Standard Test Method for Density of Powder Metallurgy (PM) Materials Containing Less Than Two Percent Porosity." https://www.astm.org/b0311-17.html (accessed May 24, 2023).
- [45] "Download." https://imagej.nih.gov/ij/download.html (accessed Nov. 21, 2022).
- [46] "Standard Test Methods for Determining Average Grain Size." https://www.astm.org/e0112-13r21.html (accessed May 23, 2023).
- [47] R. Z. Valiev, Yu. V. Ivanisenko, E. F. Rauch, and B. Baudelet, "Structure and deformation behaviour of Armco iron subjected to severe plastic deformation," *Acta Mater.*, vol. 44, no. 12, pp. 4705–4712, Dec. 1996, doi: 10.1016/S1359-6454(96)00156-5.
- [48] K. Thompson, J. H. Booske, D. J. Larson, and T. F. Kelly, "Three-dimensional atom mapping of dopants in Si nanostructures," *Appl. Phys. Lett.*, vol. 87, no. 5, p. 052108, Jul. 2005, doi: 10.1063/1.2005368.
- [49] "Standard Test Methods for Vickers Hardness and Knoop Hardness of Metallic Materials." https://www.astm.org/e0092-17.html (accessed May 23, 2023).

- [50] M. Krystýnová, P. Doležal, S. Fintová, M. Březina, J. Zapletal, and J. Wasserbauer, "Preparation and Characterization of Zinc Materials Prepared by Powder Metallurgy," *Metals*, vol. 7, no. 10, Art. no. 10, Oct. 2017, doi: 10.3390/met7100396.
- [51] J. Guo et al., "Oxygen-mediated deformation and grain refinement in Cu-Fe nanocrystalline alloys," Acta Mater., vol. 166, pp. 281–293, Mar. 2019, doi: 10.1016/j.actamat.2018.12.040.
- [52] K. Edalati, Z. Horita, T. Furuta, and S. Kuramoto, "Dynamic recrystallization and recovery during high-pressure torsion: Experimental evidence by torque measurement using ring specimens," *Mater. Sci. Eng. A*, vol. 559, pp. 506–509, Jan. 2013, doi: 10.1016/j.msea.2012.08.132.
- [53] H. Okamoto, "Comment on Mg-Zn (magnesium-zinc)," *J. Phase Equilibria*, vol. 15, no. 1, pp. 129–130, Feb. 1994, doi: 10.1007/BF02667700.
- [54] F. Meng, J. M. Rosalie, A. Singh, H. Somekawa, and K. Tsuchiya, "Ultrafine grain formation in Mg–Zn alloy by in situ precipitation during high-pressure torsion," *Scr. Mater.*, vol. 78–79, pp. 57–60, May 2014, doi: 10.1016/j.scriptamat.2014.01.036.
- [55] Y. Yan *et al.*, "Effects of the Intermetallic Phases on Microstructure and Properties of Biodegradable Magnesium Matrix and Zinc Matrix Prepared by Powder Metallurgy," *Mater. Trans.*, vol. 59, no. 11, pp. 1837–1844, Oct. 2018, doi: 10.2320/matertrans.M2018142.
- [56] Y. Liu, W.-C. Hu, D.-J. Li, X.-Q. Zeng, and C.-S. Xu, "Theoretical predictions of the structural and thermodynamic properties of MgZn2 Laves phase under high pressure," *Appl. Phys. A*, vol. 115, no. 1, pp. 323–331, Apr. 2014, doi: 10.1007/s00339-013-7822-0.
- [57] S. Liu, G. Esteban-Manzanares, and J. LLorca, "First-principles analysis of precipitation in Mg-Zn alloys," *Phys. Rev. Mater.*, vol. 4, no. 9, p. 093609, Sep. 2020, doi: 10.1103/PhysRevMaterials.4.093609.
- [58] C.-J. Deng, M. L. Wong, M. W. Ho, P. Yu, and D. H. L. Ng, "Formation of MgO and Mg—Zn intermetallics in an Mg-based composite by in situ reactions," *Compos. Part Appl. Sci. Manuf.*, vol. 36, no. 5, pp. 551–557, May 2005, doi: 10.1016/j.compositesa.2004.09.001.
- [59] K. Edalati, A. Yamamoto, Z. Horita, and T. Ishihara, "High-pressure torsion of pure magnesium: Evolution of mechanical properties, microstructures and hydrogen storage capacity with equivalent strain," *Scr. Mater.*, vol. 64, no. 9, pp. 880–883, May 2011, doi: 10.1016/j.scriptamat.2011.01.023.
- [60] R. B. Figueiredo, K. Edalati, and T. G. Langdon, "Effect of creep parameters on the steady-state flow stress of pure metals processed by high-pressure torsion," *Mater. Sci. Eng. A*, vol. 835, p. 142666, Feb. 2022, doi: 10.1016/j.msea.2022.142666.
- [61] D. Hull and D. J. Bacon, "Chapter 3 Movement of Dislocations," in *Introduction to Dislocations (Fifth Edition)*, D. Hull and D. J. Bacon, Eds., Oxford: Butterworth-Heinemann, 2011, pp. 43–62. doi: 10.1016/B978-0-08-096672-4.00003-7.
- [62] N. X. Zhang, M. Kawasaki, Y. Huang, and T. G. Langdon, "Microstructural evolution in two-phase alloys processed by high-pressure torsion," *J. Mater. Sci.*, vol. 48, no. 13, pp. 4582–4591, Jul. 2013, doi: 10.1007/s10853-012-7087-6.
- [63] M. Kawasaki, J. Foissey, and T. G. Langdon, "Development of hardness homogeneity and superplastic behavior in an aluminum–copper eutectic alloy processed by high-pressure torsion," *Mater. Sci. Eng. A*, vol. 561, pp. 118–125, Jan. 2013, doi: 10.1016/j.msea.2012.10.096.